Electrodeposition of bactericidal and bioactive nano-hydroxyapatite onto electrospun piezoelectric polyvinylidene fluoride scaffolds

Pedro J. G. Rodrigues[1], Conceição de M. V. Elias[2], Bartolomeu C. Viana[1,3], Luciana M. de Hollanda[4,5], Thiago D. Stocco[5,6], Luana M. R. de Vasconcellos[7], Daphne de C. R. Mello[7], Francisco E. P. Santos[1,3], Fernanda R. Marciano[3], Anderson O. Lobo[1,a)] ⓘD

[1]LIMAV — Interdisciplinary Laboratory for Advanced Materials, BioMatLab Group, Materials Science & Engineering Graduate Program, UFPI — Federal University of Piauí, 64049-550 Teresina, Piauí, Brazil
[2]Instituto Científico e Tecnológico, Universidade Brasil, 08230-030 São Paulo, Brazil
[3]Department of Physics, UFPI — Federal University of Piauí, 64049-550 Teresina, PI, Brazil
[4]Universidade UniMetrocamp, 13035-500 Campinas, São Paulo, Brazil
[5]Faculty of Medical Sciences, State University of Campinas, 13083-970 Campinas, São Paulo, Brazil
[6]University of Santo Amaro, 04829-300 São Paulo, Brazil
[7]Department of Bioscience and Oral Diagnosis, Institute of Science and Technology, Sao Paulo State University, 12247-004 Sao Jose dos Campos, Sao Paulo, Brazil
a)Address all correspondence to this author. e-mail: lobo@ufpi.edu.br

The fibrous scaffolds for bone tissue engineering that mimic the extracellular matrix with bioactive and bactericidal properties could provide adequate conditions for regeneration of damaged bone. Electrospun ultrathin fiber covered with nano-hydroxyapatite is a favorable fibrous scaffold design. We developed a fast and reproducible strategy to produce polyvinylidene fluoride (PVDF)/nano-hydroxyapatite (nHAp) nanofibrous scaffolds with bactericidal and bioactive properties. Fibrous PVDF scaffolds were obtained first by the electrospinning method. Then, their surfaces were modified using oxygen plasma treatment followed by electrodeposition of nHAp. This process formed nanofibrous and superhydrophilic PVDF fibers (133.6 nm, fiber average diameter) covered with homogeneous nHAp (202.6 nm, average particle diameter) crystals. Energy-dispersive X-ray spectrometry demonstrated the presence of calcium phosphate, indicating a Ca/P molar ratio of approximately 1.64. X-ray diffraction, Fourier transform infrared spectroscopy, and Raman spectroscopy spectra identified β-phase of nHAp. Thermal analysis indicated a slight reduction in stability after nHAp electrodeposition. Bactericidal assays showed that nHAp exhibited 99.8% efficiency against *Pseudomonas aeruginosa* bacteria. The PVDF/Plasma and PVDF/nHAp groups had the highest cell viability, total protein, and alkaline phosphatase activity by 7 days after exposure of the scaffolds to MG63 cell culture. Therefore, the developed scaffolds are an exciting alternative for application in bone regeneration.

Introduction

Ultrathin fibrous scaffolds have been used as bioactive components [1, 2], but the rate of bacterial contamination is a concern. Nevertheless, emerging biomaterials could have bioactive properties and promote bone tissue growth reducing bacterial growth. The bacterial proliferation can be drastically reduced when cultivated on polymeric surfaces due to hydrophobicity, surface charge, chemical composition, surface roughness, topography, or physical configuration [3, 4].

Many studies have attempted to incorporate nano-hydroxyapatite (nHAp) particles into piezoelectric polymeric matrices [5, 6]. However, those strategies slowly make nHAp available to the organism because polymer degradation is necessary. Thus, the incorporation of nHAp outside the fiber is a critical challenge, and many methods have been published with polymers such as poly-L-lactic acid (PLLA), poly (butyleneadipate-co-terephthalate) (PBAT), polypyrrole (PPy), and polycaprolactone (PCL) [7, 8, 9].

Piezoelectric materials have attracted growing interest in regenerative medicine, since they can be configured to implantable active interfaces, transmitting electrical stimulation during the mechanical impulse, thus improving tissue regeneration [10, 11]. Among the various fabrication techniques available, electrospinning is the most effective method to produce three-dimensional fibrous and piezoelectric scaffolds in a single step [12] to resemble the structure of the bone extracellular matrix. This simple approach, coupled with the easy incorporation of functional components, makes it an excellent technique for applications in bone tissue engineering (BTE) [13, 14].

Polyvinylidene fluoride (PVDF), a semicrystalline polymer, is attractive due to its piezoelectric efficiency, biocompatibility, and easy processability [15]. This polymer has a higher piezoelectric response than other polymers, such as nylon, polylactic acid, and polyhydroxybutyrate [16]; however, few studies have dynamically explored the potential of PVDF for bone regeneration [17, 18]. However, hydrophobicity of PVDF limits cell attachment and growth [12].

In BTE, nHAp is one of the most used biomaterials, due to its bioactive properties, osteoconductivity, and chemical and crystallographic similarities with natural bone [19]. Several biomaterials have been developed for autografts or allografts, including nHAp inside scaffolds for bone repair [20, 21, 22] Conductive piezoelectric fibers could be considered an interesting scaffold to grown nHAp using the electrodeposition method. Electrodeposition is a fast, simple, low-cost, and reproducible method [8]. Few studies have investigated the homogeneous covering of ultrathin fibers of conductive and piezoelectric polymers with nHAp using the electrodeposition technique [23, 24]. In previous studies, our research group electrodeposited nHAp onto superhydrophilic porous poly-D, L-lactic acid/carbon nanotube membranes, and PBAT/PPy ultrathin fibers [25, 26].

Herein, we develop nanofibrous, bioactive, and bactericidal scaffolds based on PVDF covered with electrodeposited nHAp crystals. Electrospinning and electrophoretic depositions were employed to create this new nanobiomaterial. The gram-positive and -negative bacterial growth was reduced considerably. Cultivated osteoblasts demonstrated the improved *in vitro* calcium deposition and alkaline phosphatase of this material. Our strategy is very attractive to biomaterials science because it associates a bioactive scaffold with bactericidal properties, avoiding cross-contamination and antibiotics after bone grafts.

Results

Figure 1 shows the micrographs of ultrathin PVDF, PVDF (PLASMA), and PVDF/nHAp (nHAp obtained by electrodeposition) fibrous scaffolds. The average diameter of the PVDF scaffolds [Figs. 1(a) and 1(b); 133 ± 0.03 nm] was more significant than that after plasma treatment (Plasma) [Figs. 1(c) and 1(d); 103.6 ± 0.018 nm], but all were ultrafine fibers. This measurement is essential, because nanometric fibers demonstrate the potential to influence the biological interaction of the biomaterial [27].

Figure 1(c) illustrates the change in the texture and roughness of the PVDF fiber surfaces after the effect of the plasma treatment. Correia et al. [28] discussed that electrospun ultrathin fibers treated with O_2 plasma present small "reliefs" on the surface of the fibers, leading to eventual reduction in the number of fibers, which is probably related to the plasma treatment and the incorporation of oxygen groups onto the surface of the mats. Despite the surface effects, no significant reductions in mean diameter were found for fibers treated with O_2 plasma. In addition, no complete fusion of the fibers was detected after the treatment, as open spaces remained between the fibers in the mats [28]. Figure 1(e) elucidates the growth of a uniform nHAp layer onto the scaffold surfaces with a good distribution of the crystals, demonstrating that the electrodeposition technique was efficient for the nanocomposite production. Details of nHAp crystals are shown in high-resolution scanning electron microscopy (SEM) image [Fig. 1(g)]. Figure 1(f) charts the behavior of the average current density over time during nHAp electrodeposition. The PVDF/nHAp scaffolds obtained current density 12× higher than PVDF scaffolds.

The energy-dispersive X-ray spectrometry (EDS) spectrum [Fig. 1(f.1)] shows the presence of calcium, phosphorus, and oxygen, evidencing the electrodeposited nHAp crystals onto PVDF ultrafine fiber scaffolds. The atomic Ca/P ratio = 1.64 was calculated (using the stoichiometric formula $Ca_{10}(PO_4)_6(OH)_2$) using the results obtained from EDS spectra [Fig. 1(f.1), inside Fig. 1(f)]. These values are according to the Ca/P ratio = 1.63 of normal bone [29].

Figure 2(a) illustrates that PVDF is a hydrophobic polymer with a water contact angle of 105°. However, PVDF surfaces had a hydrophilic behavior after O_2 plasma treatment [Fig. 2(b), contact angle = 35°] and a superhydrophilic behavior after 5 min (Supplementary Video 1).

Figure 3(a) contains the X-ray diffraction (XRD) patterns of the PVDF, PVDF (Plasma), and PVDF/nHAp scaffolds. The PVDF spectrum presents an intense peak at $2\theta = 20.6°$, corresponding to the 200/010 plane reflections of β-phase, which indicate coexistence in the PVDF fibers [30]. In the diffractogram of the PVDF (Plasma), the peak at $2\theta = 20.6°$, corresponding to the 200/010 planes of β-phase, slightly decreased.

Raman spectra obtained from all analyzed groups [Fig. 3(b)] contained typical bands attributed to PVDF and nHAp. Raman spectroscopy has been used in an increasing number of scientific studies [31, 32]. The main region of the Raman spectrum for
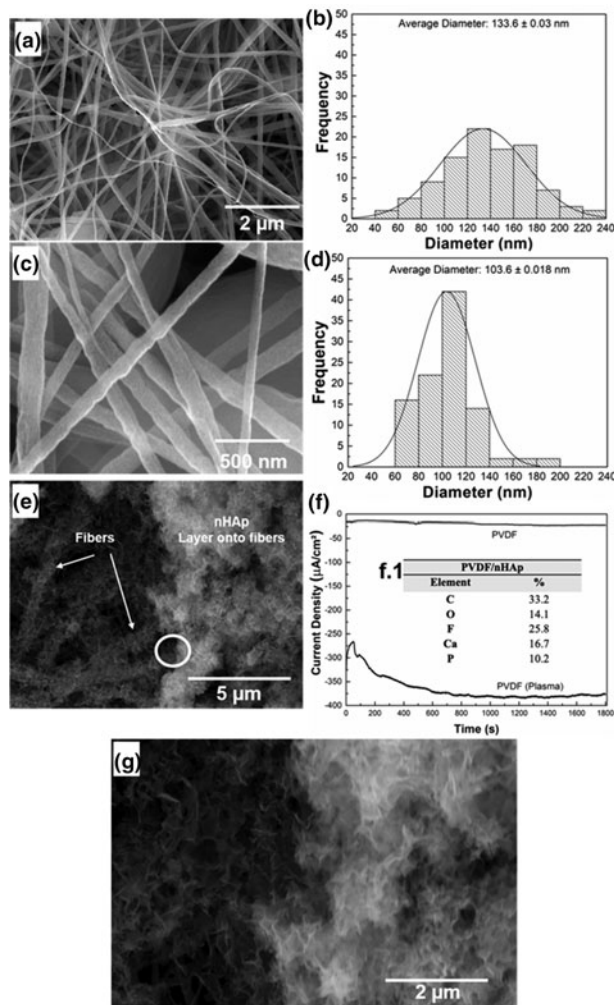
Figure 1: SEM micrographs of the scaffolds: (a) PVDF, (c) PVDF (PLASMA), (e) PVDF/nHAp (details of fibers and nHAp crystals described in the figure; circle showing details of nHAp crystals in high resolution (g); the ultrathin fibers of the PVDF and PVDF (PLASMA) scaffolds exhibited average diameter, calculated by the Image J program, of (b) 133.6 ± 0.03 nm and (d) 103.6 ± 0.018 nm, respectively. (f) Current density curve over time during nHAp electrodeposition. (f.1) EDX of the PVDF/nHAp scaffolds containing their chemical composition, with a Ca/P ratio of stoichiometric nHAp at 1.64. (g) High resolution image showing details of nHAp crystals (circle in (e)).
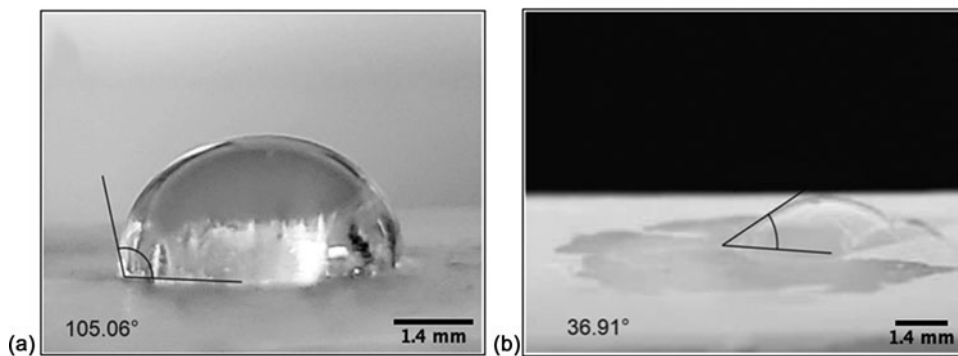

Figure 2: Measurements of the contact angle with water in PVDF scaffolds: (a) before and (b) after O_2 plasma treatment.

PVDF was between 700 and 900 cm^{-1}. PVDF modes can be seen at 488 and 611 cm^{-1} and are addressed to carbon-fluorine (CF_2) vibrations. The modes at 513 cm^{-1} are attributed to CF_2 bending vibration and 839 cm^{-1} to combination of CH_2 rocking and CF_2 stretching mode. These modes are addressed to β-phase or form I of PVDF, where to all-*trans* conformation of the PVDF chains can be attributed. Raman band at 796 cm^{-1} corresponds to the α-phase [33].
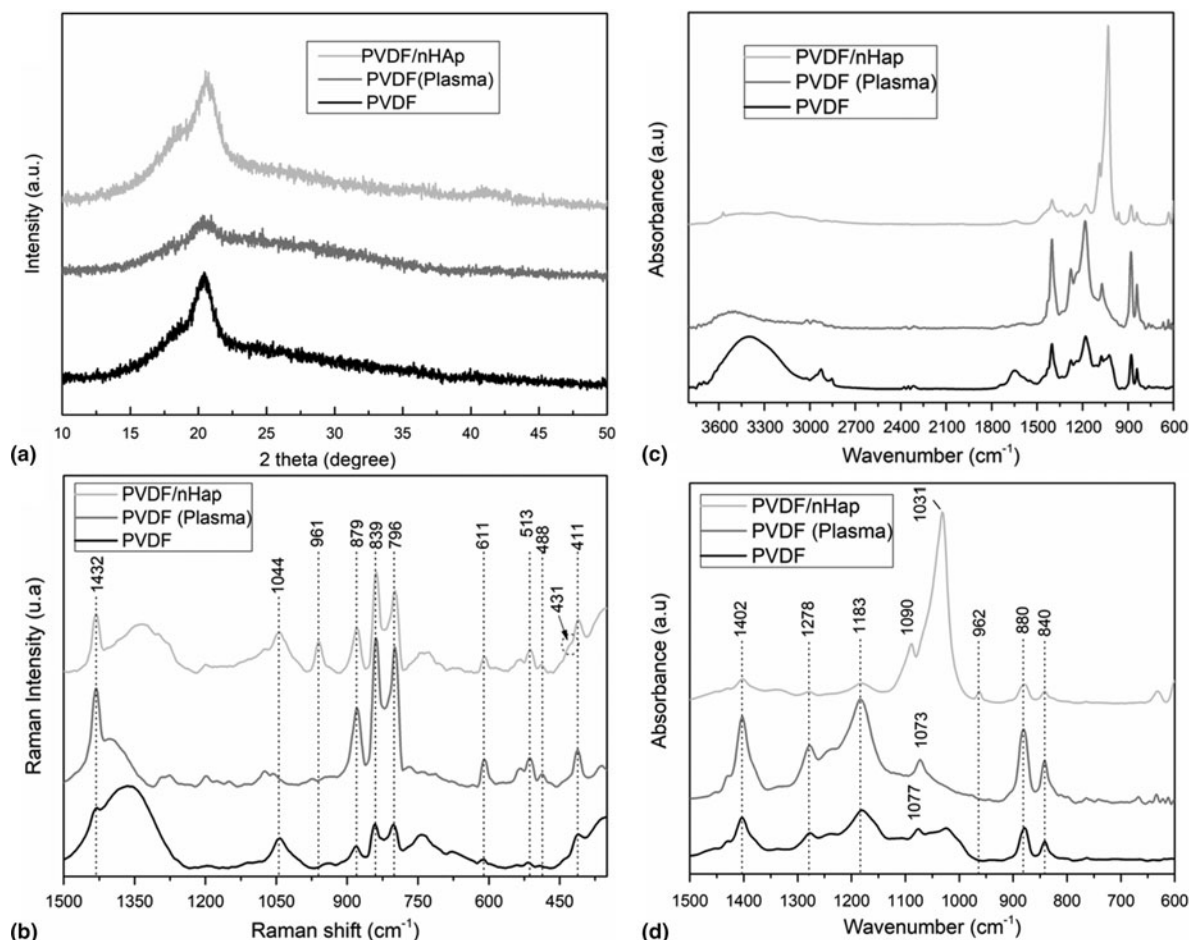
Figure 3: (a) XRD analysis for PVDF, PVDF (PLASMA), and PVDF/nHAp samples; (b) Raman Spectroscopy spectra of PVDF, PVDF (PLASMA), and PVDF/nHAp nano-composites; (c) ATR-FTIR spectra of PVDF, PVDF (PLASMA), and PVDF/nHAp, (d) ATR-FTIR zoom at 1500–580 cm^{-1} to 1300–580 cm^{-1} of the PVDF, PVDF (PLASMA), and PVDF/nHAp scaffolds.

Attenuated total reflectance (ATR)-Fourier transform infrared spectroscopy (FTIR) spectra of the PVDF, PVDF (Plasma), and PVDF/nHAp scaffolds [Fig. 3(c)] showed a characteristic peak attributed to PVDF polymer. According to the previous studies [34, 35], the uniaxial stretching of PVDF films results in the appearance of the β-phase, which was confirmed. Figure 3(d) illustrates the ATR-FTIR spectra of the scaffolds in the range of 1500–600 cm^{-1}. These bands could be attributable to different functional groups of the molecules. As seen in the PVDF spectra, characteristic bands appeared at 880 and 1183 cm^{-1}, which are attributed to the nonpolar α-phase of the PVDF vibration [36]. The bands at 840 cm^{-1} (r(CH$_2$)-vα (CF$_2$)) [37], 1073 cm^{-1} (vα(CC)-w(CF$_2$)+ w(CH$_2$)), and 1, 404 cm^{-1} (w(CH$_2$)-vα(CC)) [38] can be assigned to PVDF polar β-phase [37]. The band centered at 840 cm^{-1} corresponds to the electroactive dipoles perpendicular to the polymer structure in the application of a high electric field. During this process, the stretching and alignment of the ultrathin fibers slide [37]. The band centered at 880 cm^{-1} is due to the vibration of the C–F bond and flexion of the CH$_2$ bond, characterized by

the conformation of the *trans*-gauche-*trans*-gauche' (TGTG') chain [39]. The 1,073 cm^{-1} band represents the C–F bond without planar deformation characteristic of phase B [40]. The band at 1,183 cm^{-1} represents the C–C bond of PVDF [41]. The 1, 404 cm^{-1} band is related to the orientation of the molecular chain, which favors the alignment of fibers along the longitudinal axis with perpendicular electroactive dipoles [42].

The effect of nHAp particles on the thermal stability of the PVDF matrix was studied. Figures 4(a) and 4(b) show typical lines of the thermogravimetry analysis (TGA) and DTA thermograms for the pure PVDF and PVDF/nHAp matrix, respectively. The loss of adsorbed water is visible for the two analyzed scaffolds in the range of 38–100 °C. Between 212 °C and 450 °C for the PVDF/nHAp scaffold curve, the stage is assigned to the elimination of interstitial water, in addition to CO_2 adsorbed, CO_3^{-2}, and HPO_4^{-2} representing a loss of about 8% [21, 43].

Figure 5 describes the bacterial effect of PVDF, PVDF/Plasma, and PVDF/nHAp scaffolds against the *Pseudomonas aeruginosa* bacteria, which is prominent in the hospital environment [44]. This is a common gram-negative rod-shaped
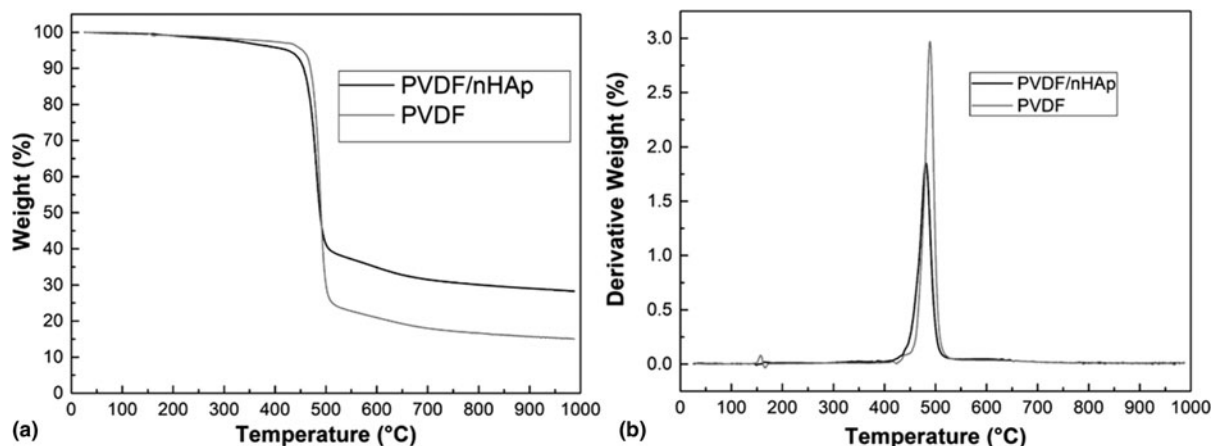
Figure 4: (a) TGA and (b) DTA curves of the PVDF and PVDF/nHAp scaffolds.
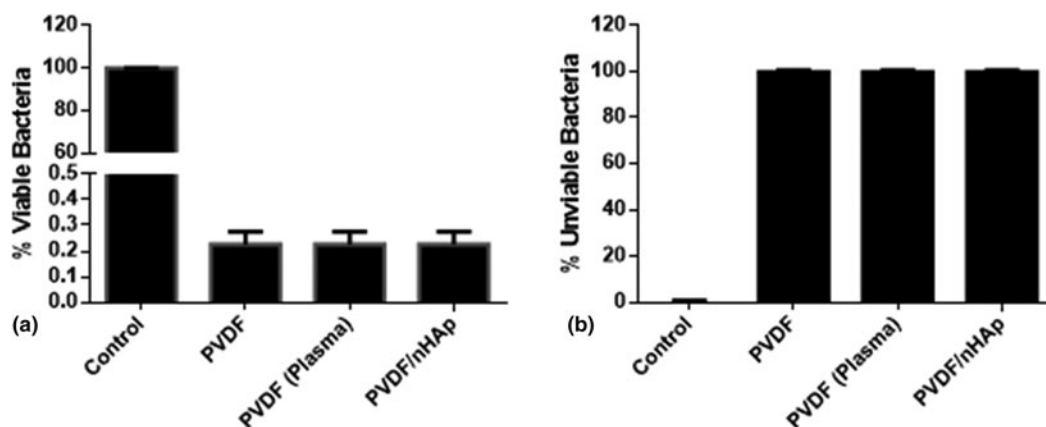

Figure 5: Bactericidal assay showing the percentage in proliferation of (a) viable bacteria and (b) unviable bacteria.

bacteria system [45]. In addition, pseudomonas infections are complicated and can be deadly. The results showed that 0.22% of the bacteria survived [Fig. 5(a)] and 99.88% died in the presence of scaffolds [Fig. 5(b)]. Similar results were founded for all materials tested without a statistical difference ($P > 0.05$). The presence of nHAp did not significantly increase the antimicrobial activities of the ultrathin fibers compared with the nonelectrodeposited nHAp. The concentration of viable bacteria was reduced by 99.8% [Fig. 5(b)] for all ultrathin scaffolds. However, the PVDF, PVDF/Plasma, and PVDF/nHAp scaffolds had an approximate conservation with 100% unviable bacteria.

Figure 6 illustrates the cell viability test [3-(4,5-dimethylthiazol-2-yl)-2,5-diphenyltetrazoliumbromide, MTT], total protein, and alkaline phosphatase (ALP) activity 7 days after the scaffolds were exposed to MG63 cell culture. The highest cell viability was observed for PVDF (Plasma) and PVDF/nHAp groups where it showed a statistical difference compared with control ($P > 0.05$), but PVDF/nHAp did not show a statistical difference ($P > 0.05$) compared with PVDF and control groups [Fig. 6(a)] (more than 70%).

Discussion

The electrodeposition process of nHAp first involves an evolution of hydroxyl ions next to scaffold surfaces, promoting an acid–base reaction to form HPO_4^{2-} and PO_4^{3}, which facilitates the precipitation of calcium phosphate onto PVDF scaffolds [8]. After that, the electrodeposition of nHAp was controlled by diffusion to form a dense layer, as observed in Fig. 1(e) [46]. The oxygen plasma improves the hydrophilic property of PVDF by introducing the oxygen containing polar groups on the surface [47]. Several research reports have noted changes in surface biocompatibility for cell attachment and protein adsorption upon plasma treatment [48].

The modification of polymers by O_2-plasma treatment introduces some hydrophilic groups. Consequently, this treatment was designed to assess the influence of wettability, topography, and cell behavior on the surface [49]. The surface topography was slightly altered under these treatment conditions [Fig. 1(c)]. Previous results revealed that cell adhesion on PVDF samples significantly improved in hydrophilic scaffold, showing about twice the scattering areas as cells grown on untreated hydrophobic scaffolds [50].
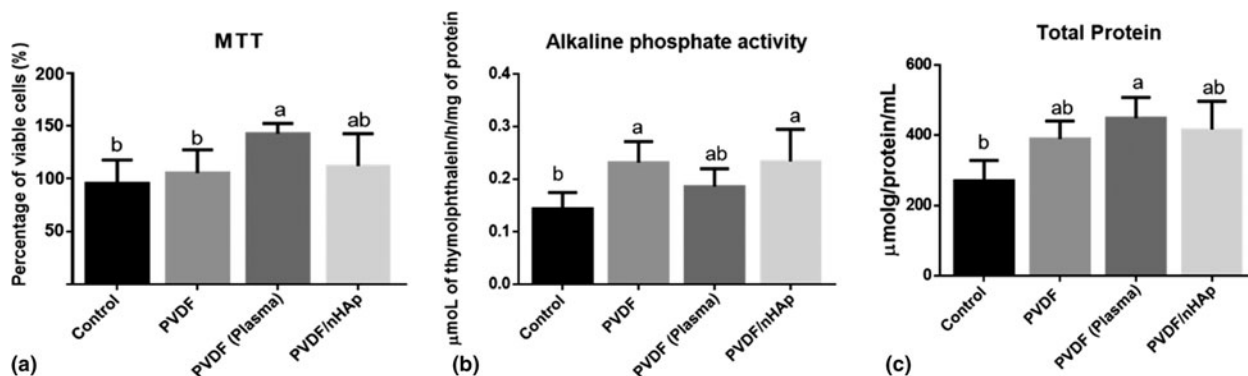
Figure 6: The effect of the sample on osteoblast behavior: (a) MTT; (b) total protein; (c) alkaline phosphate activity. The letters indicate statistical difference between the groups.

The decrease of the β-phase [Fig. 3(a)] content may be related to the local increase in the temperature of the scaffolds during treatment with O_2 plasma, leading to the transformation of the β-phase to α-phase [51]. The application of O_2 plasma on different polymeric substrates had generated promising results in promoting cell growth, due to the incorporation of hydrophilic and oxygenated functional groups [52].

However, in the diffractogram of the PVDF/nHAp scaffolds [Fig. 3(a)], no significant change was detected in the crystalline structure of the composite membranes in relation to the pure PVDF at the peak at 2θ = 20.6°. Therefore, the presence of the very low intense peak of characteristic nHAp phase at 38.4° [Fig. 3(a)] confirms its formation in nanometric size [53]. The typical diffraction peak of nHAp (38.4°) was practically hidden as a consequence of the mat structure obtained in the PVDF/nHAp scaffolds and the low crystallinity of nHAp [54].

As the electrodeposition of nHAp particles occurs in the PVDF solution, a peak appears at 961 cm^{-1} attributed to PO_4^{-3} group, a characteristic of nHAp [55]. The intense peak at 1044 cm^{-1} and the less intensity peak at 431 cm^{-1} are typically attributed to crystalline structures of apatite, such as octacalcium phosphate, which is only observed in crystallized hydroxyapatite [32, 56].

Analyzing the PVDF(Plasma) spectrum [Fig. 3(d)], we observed the preservation of the bands but with lower characteristic intensities than for PVDF [50]. This result was expected and supports the XRD spectrum [Fig. 3(a)]. The electrodeposition of nHAp in PVDF/nHAp scaffolds could be confirmed by ATR-FTIR. The vibrational sharp band in the region of 3000–3750 cm^{-1} [Fig. 3(c)] is characteristic of the stretching and vibration of OH^{-1} groups in the nHAp and a broadband of the adsorbed water group vibration. The vibration bands at 1100–1000 and 630–600 cm^{-1} are due to the vibration of PO_4^{-3}, referring to the crystalline phosphate phase of nHAp calcium [Fig. 3(d)] [57]. Along with Raman spectroscopy, FTIR analysis proved the addition of nHAp by the electrodeposition process.

Both samples showed thermal stability for temperatures up to 450 °C with a maximum decomposition temperature at 475 °C for the PVDF sample and 470 °C for PVDF/nHAp [Fig. 4(a)], with significant weight loss between 450 and 510 °C. This corresponds to PVDF decomposition [58] and indicates the lack of modification in the composite structure [59]. This dissolution temperature corresponds to the slope of the thermal degradation curves and is indicated as the maximum reaction rate (weight loss) temperature [60]. Enayati et al. [61] verified that the incorporation of nHAp in ultrathin fibers of PVA caused a minimum reduction at the maximum degradation temperature.

The slight shift in the differential thermal analysis (DTA) curve in the PVDF/nHAp sample [Fig. 4(b)] indicated moderately decreased thermal stability with the incorporation of nHAp. The PVDF/nHAp scaffolds degrade at a lower temperature than pure PVDF. Such interactions could weaken the PVDF side chains, reducing the maximum temperature of bulk degradation [and probably a shift as observed in Fig. 4(b)] [61].

The reduction on bacterial growth [Figs. 5(a) and 5(b)] was expected, considering that the ultrathin structure is less prone to bacterial adhesion and growth [62]. Recently, our group discussed that roughness and surface energy from PCL micro-/nanofibers reduced the gram-positive and -negative bacterial growth and adhesion [4]. Saravanan et al. [63] developed scaffolds of chitosan/nanohydroxyapatite/nano-silver particles (CS/nHAp/nAg) and biomaterials of CS/nHAp, so scaffolds with nAg showed a greater inhibition zone due to the antibacterial activity of silver. However, here we have developed a strategy without any nanoparticles, just associating the surface properties.

Similar to our cellular results [Figs. 6(a) and 6(b)], Kitsara et al. [50] also observed greater than 70% viable seed cells with PVDF materials. Total protein assays are important to evaluate cell-biomaterial contact [52]. The developed biomaterials induced the differentiation of MG63, exhibiting an immature osteoblast phenotype [Fig. 6(b)] [36]. Alkaline phosphatase

activity is an early osteoblast differential marker [64]. Figure 6 (c) demonstrates that PVDF/Plasma and PVDF/nHAp induced more ALP activity than the control ($P > 0.05$). PVDF has a piezoelectric property that promotes bone repair, and this intrinsic property could explain why the nHAp did not induce more ALP activity. However, the ALP activity of all engineered scaffolds were superior to the PCL and PLLA electrospun scaffolds [65, 66].

Conclusion

Here we presented, for the first time, the production of PVDF/nHAp nanofibrous scaffolds. Furthermore, this study demonstrated that the electrodeposition of nHAp stoichiometric crystals in PVDF was efficient and has potential application in BTE. Although nanocomposites exhibited a slight reduction in thermal stability, they had important bactericidal and bioactive properties for improved total protein and ALP expression when MG63 osteoblast cells were cultivated on the engineered scaffolds. Although more investigations are needed to verify the application of this new nanobiomaterial, the results suggest that porous PVDF/nHAp membranes are potential alternatives for bone grafts.

Experimental

Materials

For the production of polymeric solutions, PVDF pellets (Mw = 275,000 g/mol), N-dimethylformamide (DMF, Merck, 99.5%), acetone solutions (Merck, 99.5%), CH_3COCH_3, alcohol, $Ca(NO_3)_2 \cdot 4H_2O$, $(NH_4) \cdot H_2PO_4$, ammonium persulfate $((NH_4)_2S_2O_8)$, and sodium dodecyl sulfate $(NaC_{12}H_{25}SO_4)$ were obtained from Sigma-Aldrich Co. (USA).

Electrospinning of PVDF ultrathin fibers

The PVDF was dissolved in DMF (3 mL) with a concentration of 25 wt% (1 g) using a magnetic stirrer until complete dissolution. Afterward, the temperature control was turned off and acetone (1 mL) was added. The proportion of DMF/acetone solvents was 3:1. The electrospinning process was performed using a high-voltage power supply (SPELLMAN CZE 1000R, Hauppauge, NY, USA). The polymeric solution was inserted into a syringe [3 mL, BectonDicKinson (BD)] with a metal needle (65 mm—22 gauges, Intelbrás) and transferred to an infusion pump (KDS 100, KD Scientific, Holliston, MA, USA). The electrospinning process employed the following parameters: flow rate of 0.3 mL/h; distance of 12 cm between the collector and the needle; applied voltage of 14 kV; relative air humidity around 45–55%; metallic collectors covered with aluminum foil (92×78 mm), and around 120 min.

Plasma treatment of ultrathin fiber mats

The electrospun scaffolds were submitted to oxygen plasma treatment on both surfaces. The treatment process was conducted using the following parameters: 0.0012 kg/sec O_2 flow, 0.3 mbar pressure, 489–562 V voltage, 0.07–0.10 A electric current, and around 58 °C for 5 min.

Electrodeposition of nHAp on PVDF ultrathin fibers

A standard three-electrode cell (MSTAT 400 BIPOTENTIOSTAT/GALVANOSTAT, STAT 400) was used to electrodeposit nHAp crystals on PVDF scaffold. The electrolyte solutions used contained 2.5 mM of $Ca(NO_3)_2 \cdot 4H_2O$ and 1.5 mM of $(NH_4) \cdot H_2PO_4$, with pH adjusted to around 5 (automatically measured throughout the electrodeposition process using a pX1000 real-time pH meter) and the temperature adjusted to 65°. The PVDF scaffold was employed as a working electrode by inserting it inside a copper/Teflon sample holder (~0.28 cm²). A platinum rod was used as a counter electrode (5×10^{-2} m in length and 2×10^{-4} m in diameter). The Ag/AgCl (3 M KCl [aq.]) was used as a reference electrode. The electrodeposition process was carried out for 30 min.

Physical, chemical, morphological, and structural characterizations of scaffolds

The surface morphology, the shape, and the average diameters of the ultrathin fibers were characterized using a SEM (Quanta FEG 250, FEI company) coupled with EDS (Apollo–EDAX). For SEM analysis, a thin layer of gold (~10 nm) was deposited using a sputtering machine (Quorum Company, argon plasma at 2×10^{-1} mbar, and a current of 30 mA, for 2 min). The average diameter of the ultrathin fibers was measured using the ImageJ software. The micro-Raman spectra were collected using a SENTERRA system (Bruker, microscope Olympus BX50 with 20× objective), excitation laser at 785 nm wavelength, 50 mW laser output power, spectral resolution of 3–5 cm^{-1}, and a CCD camera (Andor Company) as a detector. FTIR operated in ATR [Vertex 70 System (Bruker)] was collected with a scanning range in the region from 4000 to 600 cm^{-1}. Raman and FTIR data were normalized (normalization model: divided by norm). The crystallographic planes of nHAp and PVDF were collected using an XRD (Shimadzu XRD 6000 diffractometer) equipment with Cu K$_\alpha$ radiation generated at 40 kV and 50 mA. The thermal behavior of the scaffolds were investigated by TGA and DTA (Q600 V20.9 Build TA instrument, nitrogen atmosphere at a flow rate of 100 mL/min and with a heating rate of 10 °C/min). Contact angle analysis was carried out after a drop of deionized water (2 μL) on scaffold surface using a homemade machine. The scaffolds were fixed on teflon substrates and the contact angles

were measured immediately afterwards. The pictures were obtained from a web camera, and the contact angle was analyzed using the ImageJ software. All measurements were performed in a controlled humidified atmosphere (±60%). A video was recorded of the PVDF after O_2 plasma treatment to show its superhydrophilic behavior (Supplementary Video 1).

Bactericidal assays

Bactericidal activity was assessed according to De Paula et al. [44] and ISO 20776-1:2019. Briefly, the bacteria *Pseudomonas aeruginosa* (ATCC 27853) were inoculated into Tryptic Soy Agar (TSA) by isolation and incubated at 37 °C for 24 h. The bacteria were resuspended in PBS up to 1.5×10^8 CFU/mL (Tube 0.5 of MacFarland Stands) and diluted in TSA up to 1.5×10^4. They were resuspended in PBS up to 1.5×10^8 CFU/mL (Tube 0.5 of MacFarland Stands) and diluted in TSA up to 1.5×10^4 CFU/mL. Then, scaffolds (10 mm × 10 mm × 0.5 mm) (in triplicate and previously sterilized) were placed in 24-well culture plates and individually inoculated with 1000 μL of the bacterial solution, and incubated for 24 h at 37 °C. After that, they were rinsed twice with PBS to remove any nonadherent bacteria. Next, the scaffolds were placed in individual flasks with PBS (1000 μL) and then vortexed to remove strongly adherent bacteria for 15 s. These suspensions of bacterial solution were diluted in series (10×; 100×; 1000×) and plated on TSA plates as 10 μL aliquots, in triplicate and incubated overnight (~24 h) at 37 °C. Finally, colonies were counted to calculate colony-forming units (CFUs). The data were normalized by raw PCL data to highlight the bactericidal activity of frameworks produced without the use of antibiotics.

In vitro assays

ISO-10993-5 developed all tests. MG63 osteoblast-like cells (human osteogenic sarcoma, Rio de Janeiro Cell Bank, APABCAM, Rio de Janeiro, RJ, Brazil) were cultivated using Dulbecco's modified Eagle medium (DMEM—Cultilab, Campinas, SP, Brazil) supplemented with 10% bovine fetal serum (Invitrogen, New York, NY, USA) and 1% penicillin–streptomycin (Gibco, Grand Island, NY, USA). To expand the cells, the culture medium was changed once every 2 days (37 °C in a humidified atmosphere of 5% CO_2). All the procedures were carried out as described by De Andrade et al. [67]. The scaffolds were sterilized by UV before each biological assay and incubated with a basal medium at 37 °C for 8 h. Polystyrene culture plate wells were used as negative control group.

After 7 days, the cellular viability was verified by reduction of MTT (Sigma-Aldrich) in formazan into of the MG63 cells (2×10^4 viable cells), which was in 24-well plates containing

1 mL of DMEM and the experimental materials such as PVDF, PVDF (Plasma), and PVDF/nHAp (37 °C; 5% CO_2). The well without cells was used as control. The colorimetric analysis was performed in a microplate spectrophotometer (Bio-Tek, Winooski, VT, USA) at 570 nm. The data were expressed in percentage (%) and normalized by control (considered 100%).

On day 7, the TP level was checked, when 50 μL was collected and added in triplicate into a 96-well plate, and the optic density was measured at 680 nm in a UV 1203 spectrophotometer (8582 Micronal, São Paulo, Brazil). The total protein content was calculated from a standard curve determined from bovine albumin and expressed as micrograms per milliliter.

From the same cell lysate described above, the ALP activity was determined by means of the thymolphthalein monophosphate release assay, using the commercial kit (Labtest Diagnóstica, Belo Horizonte, MG, Brazil), in accordance with the manufacturer's recommendations. Absorbance was measured at a wavelength of 590 nm in a UV 1203 spectrophotometer (8582 Micronal, São Paulo, Brazil). The results were expressed in μmol of thymolphthalein/min/mL.

Supplementary material

To view supplementary material for this article, please visit https://doi.org/10.1557/jmr.2020.302.

References

1. **X. Du, D. Wei, L. Huang, M. Zhu, Y. Zhang, and Y. Zhu**: 3D printing of mesoporous bioactive glass/silk fibroin composite scaffolds for bone tissue engineering. *Mater. Sci. Eng. C* **103**, 109731 (2019).

2. **I.A.W.B. Siqueira, M.A.F. Corat, B.d.N. Cavalcanti, W.A.R. Neto, A.A. Martin, R.E.S. Bretas, F.R. Marciano, and A.O. Lobo**: In vitro and in vivo studies of novel poly(d,l-lactic acid), superhydrophilic carbon nanotubes, and nanohydroxyapatite scaffolds for bone regeneration. *ACS Appl. Mater. Interfaces* **7**, 9385 (2015).

3. **J. Rodríguez-Hernández**: Antimicrobial/antifouling surfaces obtained by surface modification. In *Polymers Against Microorganisms Race to Efficient Antimicrobial Mater.*,

J. Rodríguez-Hernández, ed. (Springer International Publishing, Cham, 2017), pp. 95–123.

4. M.M. Machado-Paula, M.A.F. Corat, M. Lancellotti, G. Mi, F.R. Marciano, M.L. Vega, A.A. Hidalgo, T.J. Webster, and A.O. Lobo: A comparison between electrospinning and rotary-jet spinning to produce PCL fibers with low bacteria colonization. *Mater. Sci. Eng. C* **111**, 110706 (2020).

5. B. Tandon, P. Kamble, R.T. Olsson, J.J. Blaker, and S.H. Cartmell: Fabrication and characterisation of stimuli responsive piezoelectric PVDF and hydroxyapatite-filled PVDF fibrous membranes. *Molecules* **24**, 1903 (2019).

6. A.K. Dubey, R. Kinoshita, and K.I. Kakimoto: Piezoelectric sodium potassium niobate mediated improved polarization and in vitro bioactivity of hydroxyapatite. *RSC Adv.* **5**, 19638 (2015).

7. X. Han, X. Zhou, K. Qiu, W. Feng, H. Mo, M. Wang, J. Wang, and C. He: Strontium-incorporated mineralized PLLA nanofibrous membranes for promoting bone defect repair. *Colloids Surf. B* **179**, 363 (2019).

8. J.G. De Castro, B.V.M. Rodrigues, R. Ricci, M.M. Costa, A.F.C. Ribeiro, F.R. Marciano, and A.O. Lobo: Designing a novel nanocomposite for bone tissue engineering using electrospun conductive PBAT/polypyrrole as a scaffold to direct nanohydroxyapatite electrodeposition. *RSC Adv.* **6**, 32615 (2016).

9. P. Bhattacharjee, D. Naskar, T.K. Maiti, D. Bhattacharya, and S.C. Kundu: Non-mulberry silk fibroin grafted poly (Ie-caprolactone)/nano hydroxyapatite nanofibrous scaffold for dual growth factor delivery to promote bone regeneration. *J. Colloid Interface Sci.* **472**, 16 (2016).

10. P. Vaněk, Z. Kolská, T. Luxbacher, J.A.L. García, M. Lehocký, M. Vandrovcová, L. Bačáková, and J. Petzelt: Electrical activity of ferroelectric biomaterials and its effects on the adhesion, growth and enzymatic activity of human osteoblast-like cells. *J. Phys. D. Appl. Phys.* **49**, 175403 (2016).

11. G.G. Genchi, E. Sinibaldi, L. Ceseracciu, M. Labardi, A. Marino, S. Marras, G. De Simoni, V. Mattoli, and G. Ciofani: Ultrasound-activated piezoelectric P(VDF-TrFE)/boron nitride nanotube composite films promote differentiation of human SaOS-2 osteoblast-like cells. *Nanomed. Nanotechnol. Biol. Med.* **14**, 2421 (2018).

12. F. Ardeshiri, S. Salehi, M. Peyravi, M. Jahanshahi, A. Amiri, and A.S. Rad: PVDF membrane assisted by modified hydrophobic ZnO nanoparticle for membrane distillation. *Asia-Pacific J. Chem. Eng.* **13**, 1 (2018).

13. L.J. Villarreal-Gómez, J.M. Cornejo-Bravo, R. Vera-Graziano, and D. Grande: Electrospinning as a powerful technique for biomedical applications: A critically selected survey. *J. Biomater. Sci. Polym. Ed.* **27**, 157 (2016).

14. E. Dayaghi, H.R. Bakhsheshi-Rad, E. Hamzah, A. Akhavan-Farid, A.F. Ismail, M. Aziz, and E. Abdolahi: Magnesium-zinc scaffold loaded with tetracycline for tissue engineering application: In vitro cell biology and antibacterial activity assessment. *Mater. Sci. Eng. C* **102**, 53 (2019).

15. P. Martins, A.C. Lopes, and S. Lanceros-Mendez: Electroactive phases of poly(vinylidene fluoride): Determination, processing and applications. *Prog. Polym. Sci.* **39**, 683 (2014).

16. A. Wang, Z. Liu, M. Hu, C. Wang, X. Zhang, B. Shi, Y. Fan, Y. Cui, Z. Li, and K. Ren: Piezoelectric nanofibrous scaffolds as in vivo energy harvesters for modifying fibroblast alignment and proliferation in wound healing. *Nano Energy* **43**, 63 (2018).

17. C. Ribeiro, J. Pärssinen, V. Sencadas, V. Correia, S. Miettinen, V.P. Hytönen, and S. Lanceros-Méndez: Dynamic piezoelectric stimulation enhances osteogenic differentiation of human adipose stem cells. *J. Biomed. Mater. Res. A* **103**, 2172 (2015).

18. H.-G. Jeong, Y.-S. Han, K.-H. Jung, and Y.-J. Kim: Poly(vinylidene fluoride) composite nanofibers containing polyhedral oligomeric silsesquioxane–epigallocatechin gallate conjugate for bone tissue regeneration. *Nanomaterials* **9**, 184 (2019).

19. W.A. Ribeiro Neto, A.C.C. de Paula, T.M.M. Martins, A.M. Goes, L. Averous, G. Schlatter, and R.E. Suman Bretas: Poly (butylene adipate-co-terephthalate)/hydroxyapatite composite structures for bone tissue recovery. *Polym. Degrad. Stab.* **120**, 61 (2015).

20. J. Xu, X. Hu, S. Jiang, Y. Wang, R. Parungao, S. Zheng, Y. Nie, T. Liu, and K. Song: The application of multi-walled carbon nanotubes in bone tissue repair hybrid scaffolds and the effect on cell growth in vitro. *Polymers* **11**, 230 (2019).

21. M.M. Rahman, Md. Shahruzzaman, Md. S. Islam, M.N. Khan, and P. Haque: Preparation and properties of biodegradable polymer/nano-hydroxyapatite bioceramic scaffold for spongybone regeneration. *J. Polym. Eng.* **29**, 134 (2019).

22. E. Chatzipetros, P. Christopoulos, C. Donta, K.-I. Tosios, E. Tsiambas, D. Tsiourvas, E.-M. Kalogirou, and K. Tsiklakis: Application of nano-hydroxyapatite/chitosan scaffolds on rat calvarial critical-sized defects: A pilot study. *Med. Oral Pathol. Oral Cir. Bucal.* **23**, e625 (2018).

23. G.F. Santana-Melo, B.V.M. Rodrigues, E. da Silva, R. Ricci, F.R. Marciano, T.J. Webster, L.M.R. Vasconcellos, and A.O. Lobo: Electrospun ultrathin PBAT/nHAp fibers influenced the in vitro and in vivo osteogenesis and improved the mechanical properties of neoformed bone. *Colloids Surf. B* **155**, 544 (2017).

24. I.A.W.B. Siqueira, C.A.G.S. Oliveira, H. Zanin, M.A.V.M. Grinet, A.E.C. Granato, M.A. Porcionatto, F.R. Marciano, and A.O. Lobo: Bioactivity behaviour of nano-hydroxyapatite/freestanding aligned carbon nanotube oxide composite. *J. Mater. Sci. Mater. Med.* **26**, 1 (2015).

25. C.d.M.V. Elias, A.L.M. Maia Filho, L.R. da Silva, F.P.d.M. do Amaral, T.J. Webster, F.R. Marciano, and A.O. Lobo: In vivo evaluation of the genotoxic effects of poly (butylene

adipate-co-terephthalate)/polypyrrole with nanohydroxyapatite scaffolds for bone regeneration. *Materials* **12**, 1330 (2019).

26. H. Zanin, C.M.R. Rosa, N. Eliaz, P.W. May, F.R. Marciano, and A.O. Lobo: Assisted deposition of nano-hydroxyapatite onto exfoliated carbon nanotube oxide scaffolds. *Nanoscale* **7**, 10218 (2015).

27. S. Wang, S. Zhong, C.T. Lim, and H. Nie: Effects of fiber alignment on stem cells-fibrous scaffold interactions. *J. Mater. Chem. B* **3**, 3358 (2015).

28. D.M. Correia, C. Ribeiro, V. Sencadas, G. Botelho, S.A.C. Carabineiro, J.L.G. Ribelles, and S. Lanceros-Méndez: Influence of oxygen plasma treatment parameters on poly(vinylidene fluoride) electrospun fiber mats wettability. *Prog. Org. Coatings* **85**, 151 (2015).

29. J.P. Cassella, N. Garrington, T.C.B. Stamp, and S.H. Ali: An electron probe X-ray microanalytical study of bone mineral in osteogenesis imperfecta. *Calcif. Tissue Int.* **56**, 118 (1995).

30. W.A. Yee, M. Kotaki, Y. Liu, and X. Lu: Morphology, polymorphism behavior and molecular orientation of electrospun poly (vinylidene fluoride) fibers. *Polymer* **48**, 512 (2007).

31. J.D.A.S. Pereira, R.C.T. Camargo, J.C.S.C. Filho, N. Alves, M.A. Rodriguez-Perez, and C.J.L. Constantino: Biomaterials from blends of fluoropolymers and corn starch—implant and structural aspects. *Mater. Sci. Eng. C* **36**, 226 (2014).

32. N.M. Martinelli, M.J.G. Ribeiro, R. Ricci, M.A. Marques, A.O. Lobo, and F.R. Marciano: In vitro osteogenesis stimulation via nano-hydroxyapatite/carbon nanotube thin films on biomedical stainless steel. *Materials* **11**, 1555 (2018).

33. N.A. Shepelin, A.M. Glushenkov, V.C. Lussini, P.J. Fox, G.W. Dicinoski, J.G. Shapter, and A.V. Ellis: New developments in composites, copolymer technologies and processing techniques for flexible fluoropolymer piezoelectric generators for efficient energy harvesting. *Energy Environ. Sci.* **12**, 1143 (2019).

34. A. Salimi and A.A. Yousefi: FTIR studies of β-phase crystal formation in stretched PVDF films. *Polym. Test* **22**, 699 (2003).

35. P. Sajkiewicz, A. Wasiak, and Z. Goclowski: Phase transitions during stretching of poly(vinylidene fluoride). *Eur. Polym. J.* **35**, 423 (1999).

36. G. Hélary, F. Noirclère, J. Mayingi, and V. Migonney: A new approach to graft bioactive polymer on titanium implants: Improvement of MG 63 cell differentiation onto this coating. *Acta Biomater.* **5**, 124 (2009).

37. S. Janakiraman, A. Surendran, S. Ghosh, S. Anandhan, and A. Venimadhav: Electroactive poly(vinylidene fluoride) fluoride separator for sodium ion battery with high coulombic efficiency. *Solid State Ionics* **292**, 130 (2016).

38. N. Awanis Hashim, Y. Liu, and K. Li: Stability of PVDF hollow fibre membranes in sodium hydroxide aqueous solution. *Chem. Eng. Sci.* **66**, 1565 (2011).

39. D.M. Correia, J. Nunes-Pereira, D. Alikin, A.L. Kholkin, S.A.C. Carabineiro, L. Rebouta, M.S. Rodrigues, F. Vaz, C.M. Costa, and S. Lanceros-Méndez: Surface wettability modification of poly(vinylidene fluoride) and copolymer films and membranes by plasma treatment. *Polymer* **169**, 138 (2019).

40. Y. Bormashenko, R. Pogreb, O. Stanevsky, and E. Bormashenko: Vibrational spectrum of PVDF and its interpretation. *Polym. Test* **23**, 791 (2004).

41. A. Rahimpour, S.S. Madaeni, S. Zereshki, and Y. Mansourpanah: Preparation and characterization of modified nano-porous PVDF membrane with high antifouling property using UV photo-grafting. *Appl. Surf. Sci.* **255**, 7455 (2009).

42. L. Persano, C. Dagdeviren, Y. Su, Y. Zhang, S. Girardo, D. Pisignano, Y. Huang, and J.A. Rogers: High performance piezoelectric devices based on aligned arrays of nanofibers of poly (vinylidenefluoride-co-trifluoroethylene). *Nat. Commun.* **4**, 1610 (2013).

43. A. Krajewski, M. Mazzocchi, P.L. Buldini, A. Ravaglioli, A. Tinti, P. Taddei, and C. Fagnano: Synthesis of carbonated hydroxyapatites: Efficiency of the substitution and critical evaluation of analytical methods. *J. Mol. Struct.* **744–747**, 221 (2005).

44. M.M.M. De Paula, N.J. Bassous, S. Afewerki, S.V. Harb, P. Ghannadian, F.R. Marciano, B.C. Viana, C.R. Tim, T.J. Webster, and A.O. Lobo: Understanding the impact of crosslinked PCL/ PEG/GelMA electrospun nanofibers on bactericidal activity. *PLoS One* **13**, 1 (2018).

45. M.A. Jacobs, A. Alwood, I. Thaipisuttikul, D. Spencer, E. Haugen, S. Ernst, O. Will, R. Kaul, C. Raymond, R. Levy, L. Chun-Rong, D. Guenthner, D. Bovee, M.V. Olson, and C. Manoil: A genome-scale analysis for identification of genes required for growth or survival of haemophilus influenzae. *Proc. Natl Acad. Sci. USA* **99**, 966 (2003).

46. N. Eliaz, W. Kopelovitch, L. Burstein, E. Kobayashi, and T. Hanawa: Electrochemical processes of nucleation and growth of calcium phosphate on titanium supported by real-time quartz crystal microbalance measurements and X-ray photoelectron spectroscopy analysis. *J. Biomed. Mater. Res. A* **89**, 270 (2009).

47. C.M. Chan, T.M. Ko, and H. Hiraoka: Polymer surface modification by plasmas and photons. *Surf. Sci. Rep.* **24**, 1 (1996).

48. E.D. Yildirim, H. Ayan, V.N. Vasilets, A. Fridman, S. Guceri, and W. Sun: Effect of dielectric barrier discharge plasma on the attachment and proliferation of osteoblasts cultured over poly (ε-caprolactone) scaffolds. *Plasma Process. Polym.* **5**, 58 (2008).

49. L. Hao and J. Lawrence: On the role of CO_2 laser treatment in the human serum albumin and human plasma fibronectin adsorption on zirconia (MGO-PSZ) bioceramic surface. *J. Biomed. Mater. Res. A* **69**, 748 (2004).

50. M. Kitsara, A. Blanquer, G. Murillo, V. Humblot, S. De Bragança Vieira, C. Nogués, E. Ibáñez, J. Esteve, and L. Barrios:

Permanently hydrophilic, piezoelectric PVDF nanofibrous scaffolds promoting unaided electromechanical stimulation on osteoblasts. *Nanoscale* **11**, 8906 (2019).

51. **M.P. Silva, C.M. Costa, V. Sencadas, A.J. Paleo, and S. Lanceros-Méndez**: Degradation of the dielectric and piezoelectric response of β-poly(vinylidene fluoride) after temperature annealing. *J. Polym. Res.* **18**, 1451 (2011).

52. **D. Mangindaan, I. Yared, H. Kurniawan, J.-R. Sheu, and M.-J. Wang**: Modulation of biocompatibility on poly(vinylidene fluoride) and polysulfone by oxygen plasma treatment and dopamine coating. *J. Biomed. Mater. Res. A* **100A**, 3177 (2012).

53. **P.N. Chavan, M.M. Bahir, R.U. Mene, M.P. Mahabole, and R.S. Khairnar**: Study of nanobiomaterial hydroxyapatite in simulated body fluid: Formation and growth of apatite. *Mater. Sci. Eng. B Solid-State Mater. Adv. Technol.* **168**, 224 (2010).

54. **M. Öner and B. Ilhan**: Fabrication of poly(3-hydroxybutyrate-co-3-hydroxyvalerate) biocomposites with reinforcement by hydroxyapatite using extrusion processing. *Mater. Sci. Eng. C* **65**, 19 (2016).

55. **F.C. Oliveira, J.O. Carvalho, S.B.S. Gusmão, L.d.S. Gonçalves, L.M. Soares Mendes, S.A.P. Freitas, G.O.d.M. Gusmão, B.C. Viana, F.R. Marciano, and A.O. Lobo**: High loads of nano-hydroxyapatite/graphene nanoribbon composites guided bone regeneration using an osteoporotic animal model. *Int. J. Nanomed.* **14**, 865 (2019).

56. **R.Z. LeGeros**: Monographs in oral science. In *Calcium Phosphates in Oral Biology and Medicine*, R.Z. LeGeros, ed. (Karger, New York, NY, 1991).

57. **M. Zhang, A. juan Wang, J. ming Li, and N. Song**: Effect of stearic acid modified HAp nanoparticles in different solvents on the properties of Pickering emulsions and HAp/PLLA composites. *Mater. Sci. Eng. C* **79**, 255 (2017).

58. **S. Nie, J. Zeng, H. Qin, X. Xu, J. Zeng, C. Yang, and J. Luo**: Improvement in the blood compatibility of polyvinylidene fluoride membranes via in situ cross-linking polymerization. *Polym. Adv. Technol.* **30**, 923 (2019).

59. **P.T.S. Kumar, S. Srinivasan, V.K. Lakshmanan, H. Tamura, S.V. Nair, and R. Jayakumar**: Synthesis, characterization and cytocompatibility studies of α-chitin hydrogel/nano hydroxyapatite composite scaffolds. *Int. J. Biol. Macromol.* **49**, 20 (2011).

60. **C. Tsonos, H. Zois, A. Kanapitsas, N. Soin, E. Siores, G.D. Peppas, E.C. Pyrgioti, A. Sanida, S.G. Stavropoulos, and G.C. Psarras**: Polyvinylidene fluoride/magnetite nanocomposites: Dielectric and thermal response. *J. Phys. Chem. Solids* **129**, 378 (2019).

61. **M.S. Enayati, R. Esmaeely Neisiany, P. Sajkiewicz, T. Behzad, P. Denis, and F. Pierini**: Effect of nanofiller incorporation on thermomechanical and toughness of poly (vinyl alcohol)-based electrospun nanofibrous bionanocomposites. *Theor. Appl. Fract. Mech.* **99**, 44 (2019).

62. **J. Dhom, D.A. Bloes, A. Peschel, and U.K. Hofmann**: Bacterial adhesion to suture material in a contaminated wound model: Comparison of monofilament, braided, and barbed sutures. *J. Orthop. Res.* **35**, 925 (2017).

63. **S. Saravanan, S. Nethala, S. Pattnaik, A. Tripathi, A. Moorthi, and N. Selvamurugan**: Preparation, characterization and antimicrobial activity of a bio-composite scaffold containing chitosan/nano-hydroxyapatite/nano-silver for bone tissue engineering. *Int. J. Biol. Macromol.* **49**, 188 (2011).

64. **J. Lincks, B.D. Boyan, C.R. Blanchard, C.H. Lohmann, Y. Liu, D.L. Cochran, D.D. Dean, and Z. Schwartz**: Response of MG63 osteoblast-like cells to titanium and titanium alloy is dependent on surface roughness and composition. *Biomater. Silver Jubil. Compend.* **19**, 147 (1998).

65. **Y. Tang, C. Wu, Z. Wu, L. Hu, W. Zhang, and K. Zhao**: Fabrication and in vitro biological properties of piezoelectric bioceramics for bone regeneration. *Sci. Rep.* **7**, 1 (2017).

66. **M.F. Abazari, Z. Hosseini, S. Zare Karizi, S. Norouzi, M. Amini Faskhoudi, E. Saburi, S.E. Enderami, A. Ardeshirylajimi, and H. Mohajerani**: Different osteogenic differentiation potential of mesenchymal stem cells on three different polymeric substrates. *Gene* **740**, 144534 (2020).

67. **D.P. De Andrade, L.M.R. De Vasconcellos, I.C. Silva Carvalho, L.F.D.B.P. Forte, E.L. De Souza Santos, R.F. Do Prado, D.R. Dos Santos, C.A. Alves Cairo, and Y.R. Carvalho**: Titanium-35niobium alloy as a potential material for biomedical implants: In vitro study. *Mater. Sci. Eng. C* **56**, 538 (2015).